Research Article | Open Access

Microstructures

Liao *et al. Microstructures* **2026**, *6*, 2026089 **DOI:**10.20517/microstructures.2026.10

Zn-Ti-substituted M-type hexaferrites with large magnetocrystalline anisotropy and narrow ferromagnetic resonance linewidth for millimeter-wave self-biased application

Yongjie Liao[1], Qian Liu[1], Ziyang Li[1], Xiao Tan[1], Yuxin Wu[1], Houjiao Chen[1], Chang Li[1], Xin You[2], Chongsheng Wu[1], Yuanming Lai[1]

Keywords:

M-type hexaferrites, Zn^{2+}-Ti^{4+} substitution, self-biased circulators, narrow ferromagnetic resonance linewidth.

Citation: Liao, Y.; Liu, Q.; Li, Z.; Tan, X.; Wu, Y.; Chen, H.; Li, C.; You, X.; Wu, C.; Lai, Y. Zn-Ti-substituted M-type hexaferrites with large magnetocrystalline anisotropy and narrow ferromagnetic resonance linewidth for millimeter-wave self-biased application. *Microstructures* **2026**, *6*, 2026089. https://dx.doi.org/10.20517/microstructures.2026.10

Received: 19 Jan 2026 **First Decision:** 24 Mar 2026 **Revised:** 27 May 2026 **Accepted:** 9 Jun 2026 **Published:** 30 Jun 2026

Academic Editor: Huijun Li **Copy Editor:** Ping Zhang **Production Editor:** Ping Zhang

Check for updates

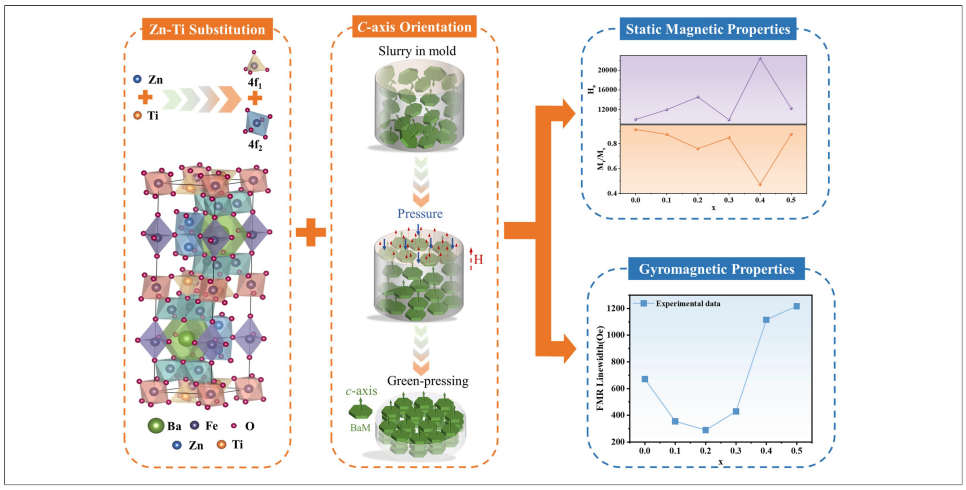

Abstract

Large magnetocrystalline anisotropy field H_a and narrow ferromagnetic resonance (FMR) linewidth ΔH are obtained for M-type hexaferrites $Ba(ZnTi)_xFe_{12-2x}O_{19}$ (BaM, x = 0.0 - 0.5) via the introduction of Zn-Ti co-substitution. Meanwhile, *c*-axis orientation provides effective access to the enhanced squareness ratio M_r/M_s. These gyromagnetic properties make the developed BaM particularly suitable as a substrate for a self-biased circulator at U band. Raman Spectroscopy indicates that Zn^{2+}-Ti^{4+} ions tend to preferentially occupy the $4f_1$ and $4f_2$ sites as x < 0.1, and then gradually spread across all available sites as x increases, which is consistent with the trend observed in saturation magnetization M_s. Outstanding magnetic properties are simultaneously achieved at x=0.1, including M_s = 55.84 emu/g, H_a = 11,930 Oe, and M_r/M_s = 0.87. In particular, the narrowest FMR linewidth (ΔH = 289 Oe at 59 GHz) is realized as x = 0.2, lower than previously reported values for BaM.

[1]School of Mechanical and Electrical Engineering, Chengdu University of Technology, Chengdu 610000, Sichuan, China.
[2]Key Laboratory of Advanced Materials of Yunnan Province, Kunming University of Science and Technology, Kunming 650000, Sichuan, China.

Correspondence to: Prof. Qian Liu, School of Mechanical and Electrical Engineering, Chengdu University of Technology, Chengdu 610000, Sichuan, China. E-mail: liuq@cdut.edu.cn

INTRODUCTION

The rapid development of active phased-array radar (APAR) and 5G massive multiple-input multiple-output (MIMO) technology has led to an increasing demand for microwave transmit/receive (T/R) modules in modern military and civilian communication systems[1,2]. In T/R modules, circulators are key non-reciprocal devices that enable unidirectional signal transmission and isolation, and their performance directly affects system stability and efficiency. Conventional circulators typically employ garnet or spinel ferrites as gyromagnetic materials and rely on external permanent magnets to provide a bias field because their magnetocrystalline anisotropy field (H_a) is insufficient. However, pushing operating frequencies into the millimeter-wave range demands significantly stronger bias fields, which in turn require permanent magnets with larger volumes and greater weight, making device planarization and integration increasingly difficult[3]. Consequently, the development of self-biased circulators that do not require or decrease the volume of external magnets has become an important research direction in microwave ferrite materials and devices. Hexaferrites are considered ideal materials for self-biased circulators due to their high magnetocrystalline anisotropy field (H_a), which can provide an equivalent internal bias field[4]. Among them, BaM hexaferrite ($BaFe_{12}O_{19}$) has attracted considerable attention because of its simple crystal structure, ease of synthesis, high Curie temperature, large saturation magnetization (M_s), and strong uniaxial anisotropy[5]. However, hexaferrite-based circulators exhibit higher insertion loss than traditional spinel or garnet-based circulators. To overcome this drawback, *c*-axis-oriented BaM polycrystalline materials are developed by magnetic-field alignment to achieve high remanence ratios (M_r/M_s) along the *c*-axis, which helps reduce low-field losses and improve circulator performance[6], as well as introducing ion substitution to regulate magnetic properties, especially for H_a and FMR linewidth ΔH.

At present, investigations into M-type hexaferrites are primarily directed toward tailoring magnetic properties through selective ionic substitution at the five distinct Fe^{3+} crystallographic sites (spin-up: 2a, 2b, 12k; spin-down: $4f_1$, $4f_2$)[7-9]. Among the various substitution strategies, introducing divalent and tetravalent cations simultaneously has proven especially effective in modulating the static and dynamic magnetic properties of hexaferrites. In this context, the Zn^{2+}-Ti^{4+} co-substitution system has attracted considerable attention due to its pronounced ability to tune key magnetic parameters, including saturation magnetization, magnetocrystalline anisotropy, and coercivity. Achieving targeted property tailoring requires a clear understanding of where exactly the substituting ions preferentially occupy within the crystal structure and how their site preferences relate to the observed changes in magnetic properties. A range of approaches has been developed for this purpose. Among these, direct experimental evidence has been provided by spectroscopic and diffraction techniques. Mössbauer spectroscopy studies by González-Angeles *et al.* demonstrated that at low substitution levels, Zn^{2+} ions preferentially occupy the tetrahedral $4f_1$ down-spin site, whereas Ti^{4+} ions exhibit a marked tendency to enter the octahedral $4f_2$ down-spin site, with a secondary preference for the 2a up-spin site at higher substitution levels[10]. This selective occupation of the spin-down sublattices by non-magnetic cations reduces the negative contribution to the net magnetization, thereby leading to an initial enhancement in saturation magnetization (M_s). Complementary neutron diffraction measurements performed by Wartewig *et al.* confirmed that nearly all Zn^{2+} cations reside on the $4f_1$ tetrahedral site. However, Ti^{4+} cations are distributed with comparable probability between the $4f_2$ and 12k octahedral sites[11]. The incorporation of non-magnetic Ti^{4+} ions into the 12k up-spin sublattice at elevated substitution levels progressively weakens the overall superexchange interactions, leading to a reduction in both the saturation magnetization and the magnetocrystalline anisotropy field (H_a). In contrast, an alternative class of studies infers ion occupation indirectly from changes in macroscopic magnetic behavior. More recently, Solizoda *et al.* investigated the aliovalent substitution of Ti^{4+} in BaM and proposed that Ti^{4+} ions primarily enter the 12k octahedral site. At the same time, the charge compensation mechanism induces partial reduction of Fe^{3+} to Fe^{2+} at the $4f_2$ site[12]. This redistribution of cation valences and the associated modification of Fe-O-Fe superexchange pathways further influence the magnetic anisotropy and contribute

to the observed reduction in coercivity.

Even with these investigations, the precise site preference of Ti^{4+} ions, especially whether they favor the $4f_2$ or the 12k site, has not yet been conclusively determined. Moreover, the existing studies have primarily focused on static magnetic properties. However, from the perspective of millimeter-wave gyromagnetic applications, a critical parameter is the ferromagnetic resonance (FMR) linewidth (ΔH), which directly dictates the intrinsic insertion loss of self-biased devices. Although the studies mentioned above offer useful insights into controlling static magnetic properties, systematic research on Zn^{2+}-Ti^{4+} co-substituted, *c*-axis-oriented BaM hexaferrites, with a specific focus on reducing the FMR linewidth, remains very limited. This study aims to synthesize *c*-axis-oriented $Ba(ZnTi)_xFe_{12-2x}O_{19}$ (x = 0.0 - 0.5 in increments of 0.1) through a high-temperature solid-state reaction combined with magnetic-field orientation. The effect of Zn^{2+}-Ti^{4+} doping on the properties of M-type hexaferrites is investigated primarily by tailoring magnetic parameters such as the anisotropy field Ha, the squareness ratio M_r/M_s, and the FMR linewidth ΔH, and exploring their potential as gyromagnetic materials for millimeter-wave self-biased circulators.

EXPERIMENTAL

A series of $Ba(ZnTi)_xFe_{12-2x}O_{19}$ samples with x = 0.0 - 0.5, in increments of 0.1, were synthesized through a high-temperature solid-state reaction, the detailed flow chart of which is presented in Figure 1. Stoichiometric ratios of raw materials, $BaCO_3$, ZnO, TiO_2, and Fe_2O_3 with a purity of 99% (MACKLIN), were weighed and transferred into six ball-milling jars. To each jar, 300 mL of deionized water was added, and the mixture was milled in a planetary ball mill at 300 rpm for 12 h. After drying at 100 °C, the mixed powders underwent pre-sintering at 1,250 °C in air for 4 h. Next, 8 wt% dispersant ($C_{21}H_{14}Na_2O_6S_2$, NNO, MACKLIN) was introduced into each batch, and a secondary milling step was performed at 500 rpm for 24 h. The resulting slurry was then poured into a mold and compacted into cylindrical bodies with a diameter of ≈30 mm and a height of ≈15 mm under a magnetic field of 10 kOe and a pressure of 4 MPa. Finally, the compacts were sintered at 1,200 °C in air for 4 h.

After the secondary ball-milling step, the particle size distribution of the resulting slurry was determined by wet laser diffraction on a Mastersizer 2000 (Malvern Panalytical, UK). The volume fraction corresponding to each particle size interval was then evaluated. According to magnetic-domain theory, the dominant magnetization mechanism in single-domain or quasi-single-domain particles is irreversible spin rotation. In the absence of domain walls, magnetic moments readily align along the crystallographically easy axis (*c*-axis) under an applied magnetic field and retain this orientation after the field is removed, thereby enabling a high remanence ratio (M_r/M_s). In comparison, multi-domain particles magnetize through irreversible domain-wall displacement accompanied by Barkhausen jumps, a process strongly influenced by internal stress fluctuations and grain-boundary effects, resulting in a weaker magnetic response that is generally unfavorable for achieving high *c*-axis orientation and remanence. Hence, controlling the particle size through the second ball-milling step to obtain a majority of single-domain or quasi-single-domain particles is crucial. According to Figure 2, particles smaller than 10.67 μm and 18.28 μm account for cumulative volume fractions of 50% and 90%, respectively. Even though most particles exceed the single-domain size threshold of < 1.3 μm[13], the overall size distribution remains relatively homogeneous. A relatively uniform particle size distribution reduces the variation in alignment resistance that typically arises from size disparities during magnetic field orientation, thereby improving overall texture quality and promoting a higher degree of *c*-axis alignment in the final material.

X-ray diffraction (XRD, D8 Advance, Bruker, Germany) was employed for phase analysis over a 2θ range of 20°-80°. Rietveld refinement was then performed to determine the lattice parameters. Field-emission scanning electron microscopy (SEM, Apreo 2C, Thermo Scientific, USA) was used to examine the

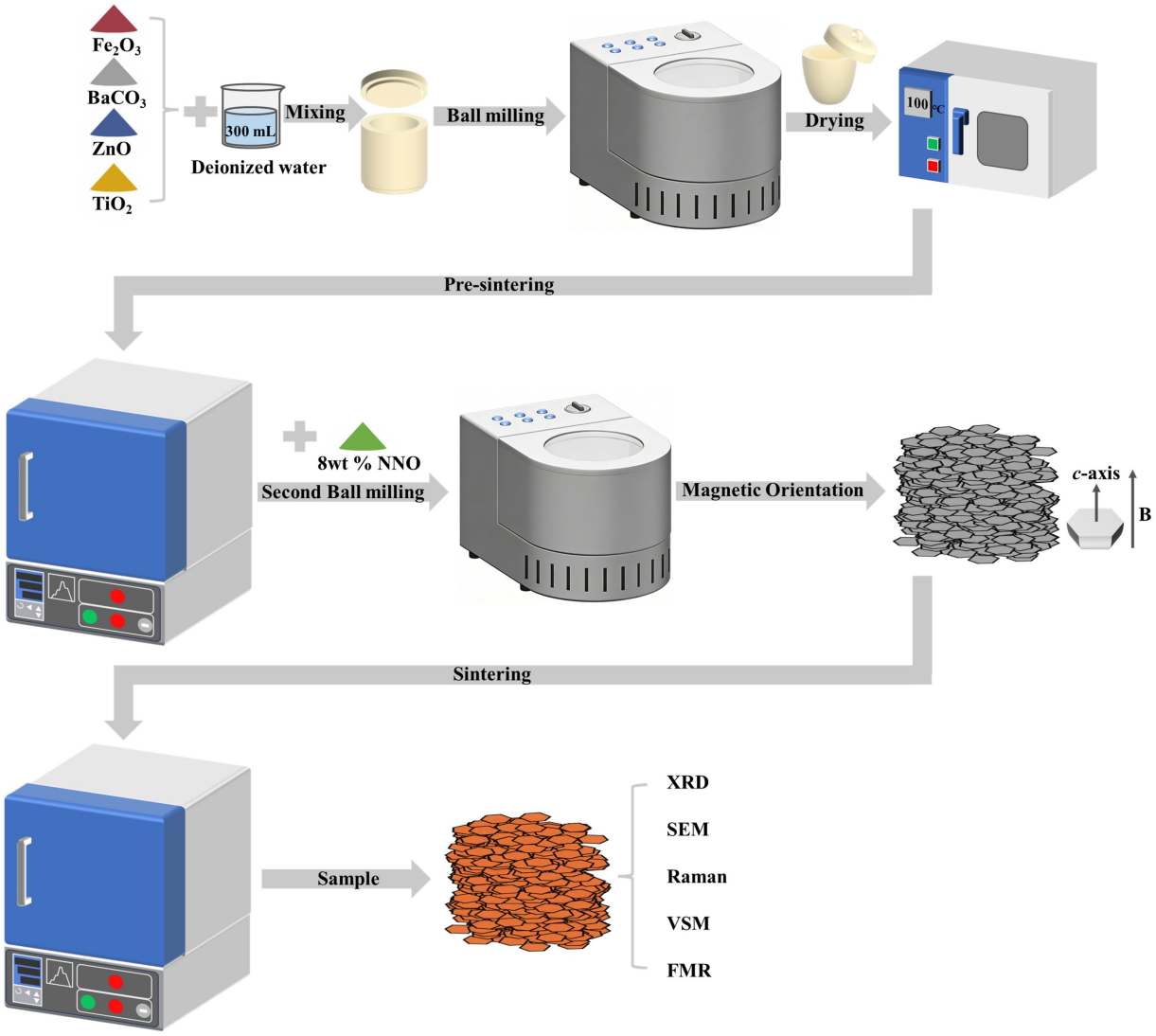

Figure 1. Preparation and magnetic field orientation process details. XRD: X-ray diffraction; SEM: scanning electron microscopy; VSM: vibrating sample magnetometer; FMR: ferromagnetic resonance.

microstructure. Raman spectroscopy (DXR3, Thermo Scientific, USA) was conducted with a 532 nm laser excitation source. Magnetic hysteresis loops were recorded using a vibrating sample magnetometer (VSM, 8600, Lake Shore, USA), with the external field oriented along the crystallographic *c*-axis. Saturation magnetization (M_s), coercivity (H_c), and remanence ratio (M_r/M_s) were determined. For FMR measurements, samples were cut into plates measuring 4.0 × 4.0 × 0.8 mm^3 and attached to a coplanar waveguide (CPW). The fixture was then carefully positioned at the geometric center of the electromagnet pole gap, ensuring the sample was exposed to a highly uniform static magnetic field throughout the measurement. Resonance absorption was detected by monitoring the S_{21} transmission parameter using a vector network analyzer (VNA, Ceyear 3674G) while a static magnetic field was applied to the sample through an electromagnet.

RESULTS AND DISCUSSION

Phase formation and microstructure

XRD patterns of oriented and non-oriented BaM (x = 0.3) are compared in Figure 3A. Both sets of diffraction peaks match well with the standard BaM-type hexaferrites pattern (PDF#27-1029), confirming the formation of a pure M-type hexaferrite phase with space group $P6_3/mmc$. After normalization to the

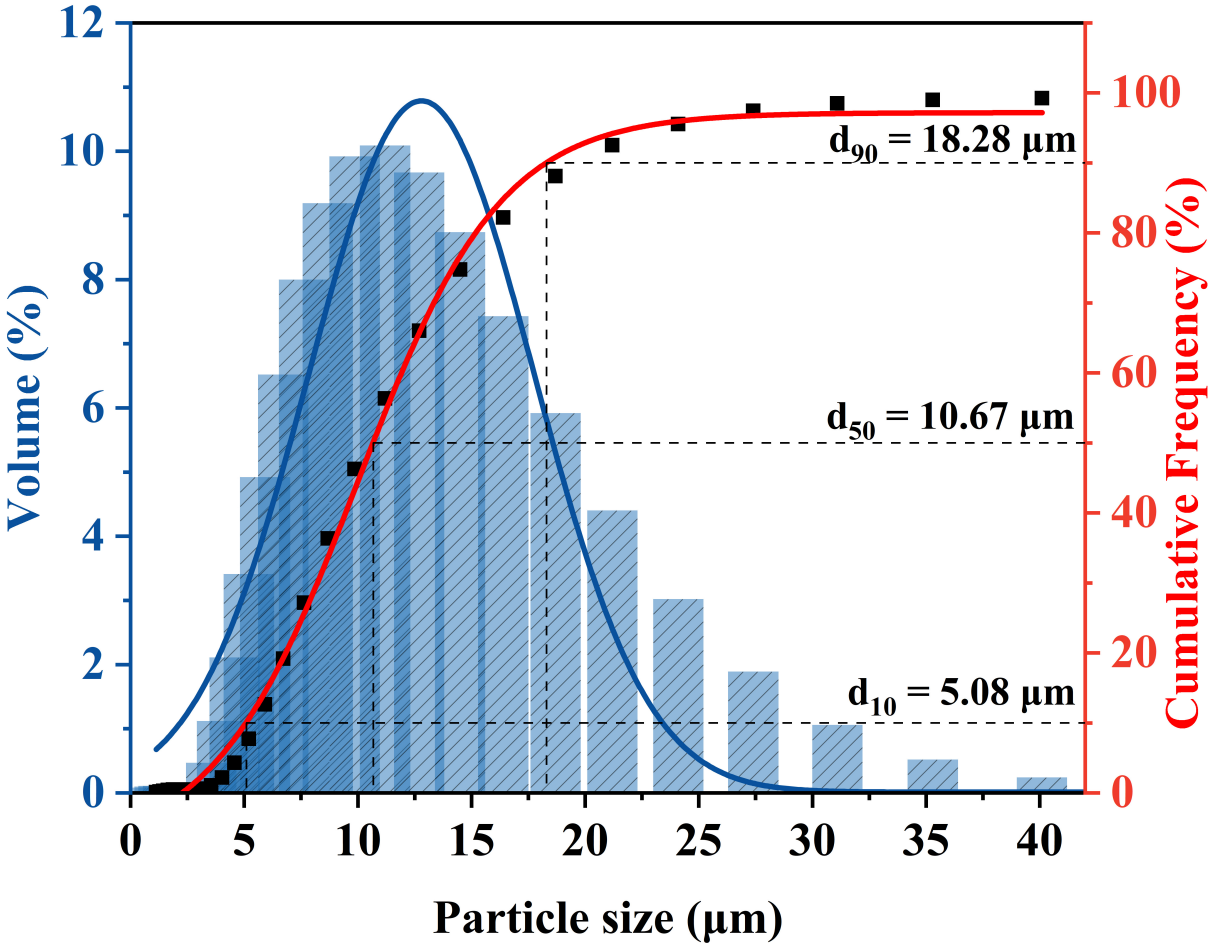

Figure 2. Particle size distribution of $Ba(ZnTi)_xFe_{12-2x}O_{19}$ (x = 0.3).

strongest peak, the oriented sample shows increased relative intensities of the (00l) reflections. Combined with the Lotgering factor f_L = 0.57 calculated from the XRD patterns, these results confirm a well-developed *c*-axis texture. Figure 3B shows XRD patterns of oriented $Ba(ZnTi)_xFe_{12-2x}O_{19}$ with different x. All samples exhibit single-phase M-type structure, but diffraction intensities vary irregularly, reaching a maximum at x = 0.3. Figure 3C displays a magnified view of the (203) peak. The ionic radius of Zn^{2+} (0.74 Å) is larger than that of Fe^{3+} (0.64 Å), while that of Ti^{4+} (0.60 Å) is smaller[14]. If ionic size alone governed the structural response, the interplanar spacing of the (203) plane would be expected to shift monotonically as the substitution level x increases. However, as shown in Figure 3C, the (203) peak exhibits a non-monotonic angular variation: it shifts progressively to higher angles for x = 0.1 - 0.3. Then it shifts back to lower angles for x = 0.4 and 0.5. The underlying mechanism responsible for this behavior involves composition-dependent site occupancy by Zn^{2+} and Ti^{4+} ions and is discussed in detail in Section 3.2, supported by Raman spectroscopy analysis. Nevertheless, the observed irregular shift of the (203) peak already confirms the successful doping of Zn^{2+} and Ti^{4+} ions into the BaM lattice.

Rietveld refinement was carried out using the General Structure Analysis System (GSAS) program. Figure 4A-F presents the Rietveld refinement patterns for all compositions, where the observed data (Obs) are shown as × symbols, the calculated profile (Cal) as a red curve, the difference curve (Obs-Cal) as a blue curve, and the Bragg peak positions (Bragg) as vertical purple tick marks. Refined lattice parameters (*a*, *c*, *c*/*a*, V_{cell}) and the corresponding goodness of fit (χ^2) are listed in Table 1. The relatively low χ^2 values confirm the

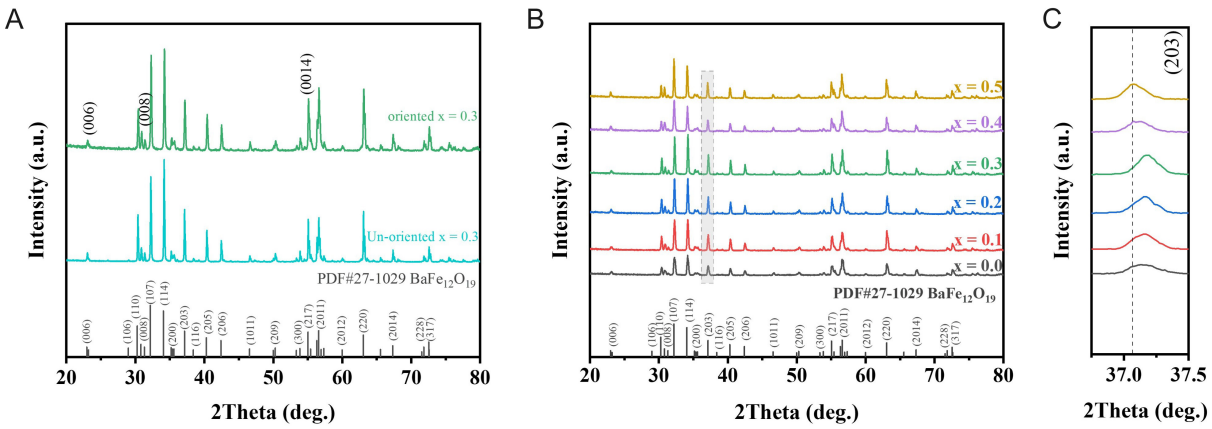

Figure 3. (A) Comparison of the oriented and non-oriented XRD patterns of BaM (x = 0.3); (B) XRD patterns of $Ba(ZnTi)_xFe_{12-2x}O_{19}$ hexaferrites; (C) Magnified view of the XRD diffraction peak of the (203) crystal plane. XRD: X-ray diffraction.

reliability of the refined lattice parameters. The *c/a* ratios are all below 3.98, confirming the hexagonal structure[15]. Notably, the lattice parameters exhibit a non-monotonic variation with increasing substitution level x. This behavior can be rationalized by the combined effects of site-occupation preference and doping level, a point that will be further clarified in Section 3.2 using Raman spectroscopy.

The Lotgering factor (f_L), defined by Equation (1) [16], provides a quantitative measure of the degree of *c*-axis texture in BaM as follows.

$$f_L = \frac{\sum I(00l)/\sum I(hkl) - \sum I_0(00l)/\sum I_0(hkl)}{1 - \sum I_0(00l)/\sum I_0(hkl)} \quad (1)$$

Here, $\sum I\,(00l)/\sum I\,(hkl)$ represents the ratio of the sum of XRD intensities from (00*l*) planes to that from all (*hkl*) planes for the oriented sample. Moreover, $\sum I_0\,(00l)/\sum I_0\,(hkl)$ is the corresponding ratio for randomly oriented BaM without preferred orientation. Based on the equation and XRD patterns, the calculated f_L values are summarized in Table 1. For instance, at x = 0.1, f_L reaches 0.57. Generally, f_L increases with a higher *c*-axis orientation[17]. While a high degree of *c*-axis orientation plays an important role in achieving a high remanence ratio, the extent of grain growth during sintering also has a strong influence on the final remanence ratio of the material. Bulk density (ρ) was determined using the drainage method of Archimedes [Table 1]. Moreover, the overall porosity (p) is defined by Equation (2) as follows[18].

$$p(\%) = 100 \times (1 - \rho/\rho_x) \quad (2)$$

$$\rho_x = \frac{ZM}{N_A V_{cell}} \quad (3)$$

In these expressions, ρ_x denotes the X-ray density as given in Equation (3)[18]. At the same time, the symbols Z, M, N_A, and V_{cell} correspond to the number of formula units per unit cell, the molecular weight, Avogadro's constant, and the unit cell volume, respectively. Previous studies have consistently shown that porosity significantly influences the FMR behavior of hexaferrites, with lower-porosity samples exhibiting narrower FMR linewidths[19]. A quantitative analysis of the FMR linewidth and its dependence on porosity is presented below.

SEM images of oriented $Ba(ZnTi)_xFe_{12-2x}O_{19}$ are presented in Figure 5A-F. The microstructural morphology shows a clear dependence on the amount of Zn^{2+} and Ti^{4+} incorporated into the BaM lattice. A typical hexagonal platelet morphology is observed across the entire sample surface, consistent with the *c/a* ratio

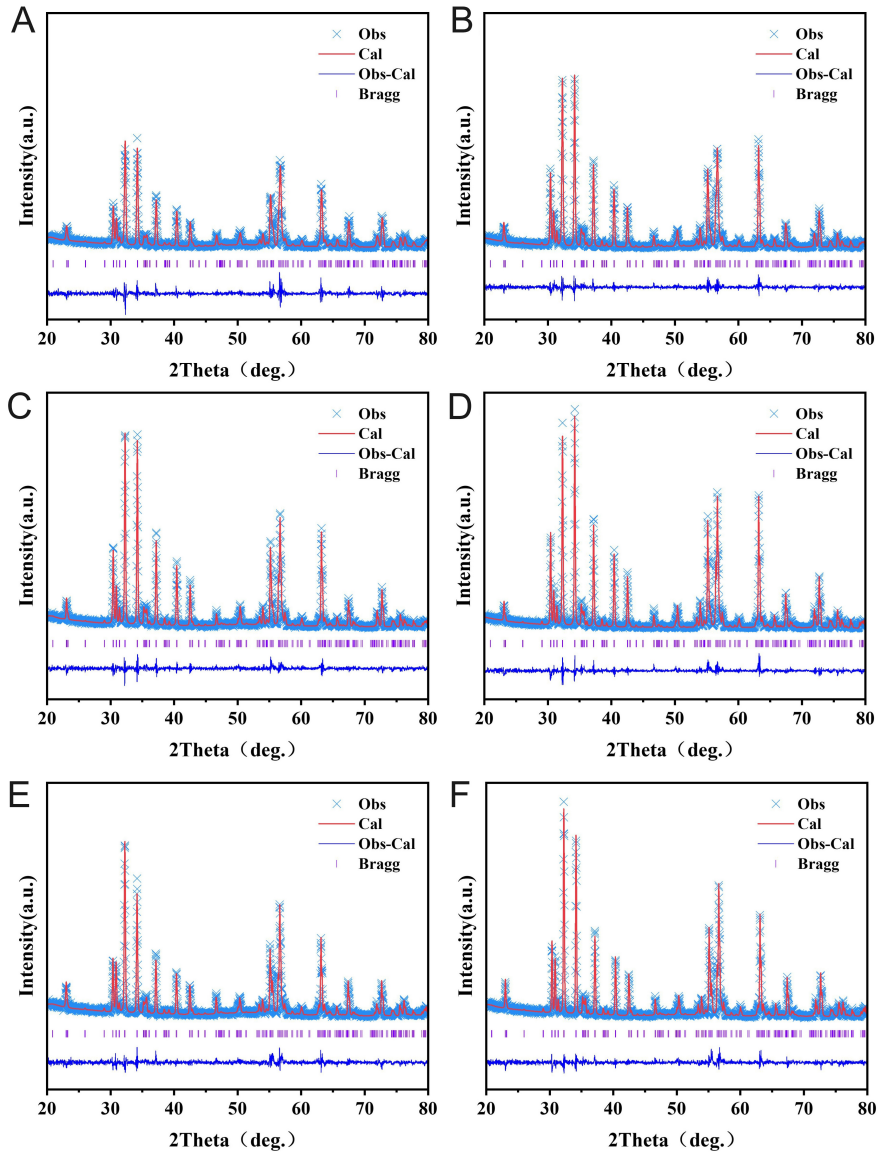

Figure 4. Rietveld refined XRD pattern of $Ba(ZnTi)_xFe_{12-2x}O_{19}$: (A) x = 0.0, (B) x = 0.1, (C) x = 0.2, (D) x = 0.3, (E) x = 0.4 and (F) x = 0.5. XRD: X-ray diffraction.

Table 1. Lattice parameters, goodness of fit, and texture metrics of all samples

x	Lattice parameters				Goodness of fit	Texture metrics		
	a (Å)	*c* (Å)	*c*/*a*	V_{cell} (Å)	χ^2	f_L	ρ (g/cm³)	*p* (%)
0.0	5.8901 (6)	23.1942 (1)	3.9378	696.89 (7)	1.51	0.57	4.72	7.39
0.1	5.8904 (2)	23.1919 (5)	3.9372	696.87 (4)	1.35	0.57	4.73	7.21
0.2	5.8898 (1)	23.1857 (7)	3.9365	696.55 (6)	1.30	0.59	4.75	6.91
0.3	5.8876 (7)	23.1696 (3)	3.9353	696.56 (4)	1.36	0.49	4.56	10.50
0.4	5.8908 (0)	23.1900 (5)	3.9366	696.91 (8)	1.42	0.48	4.30	15.68
0.5	5.8919 (2)	23.1960 (5)	3.9369	697.36 (2)	1.34	0.47	4.14	18.70

obtained from XRD refinement. Moreover, no obvious agglomeration is observed in the SEM images, resulting in a compact microstructure. The sample with x = 0.1 shows the most uniform distribution of hexagonal grains with minimal inter-grain voids. As shown in the cross-sectional images in Figure 5G and H,

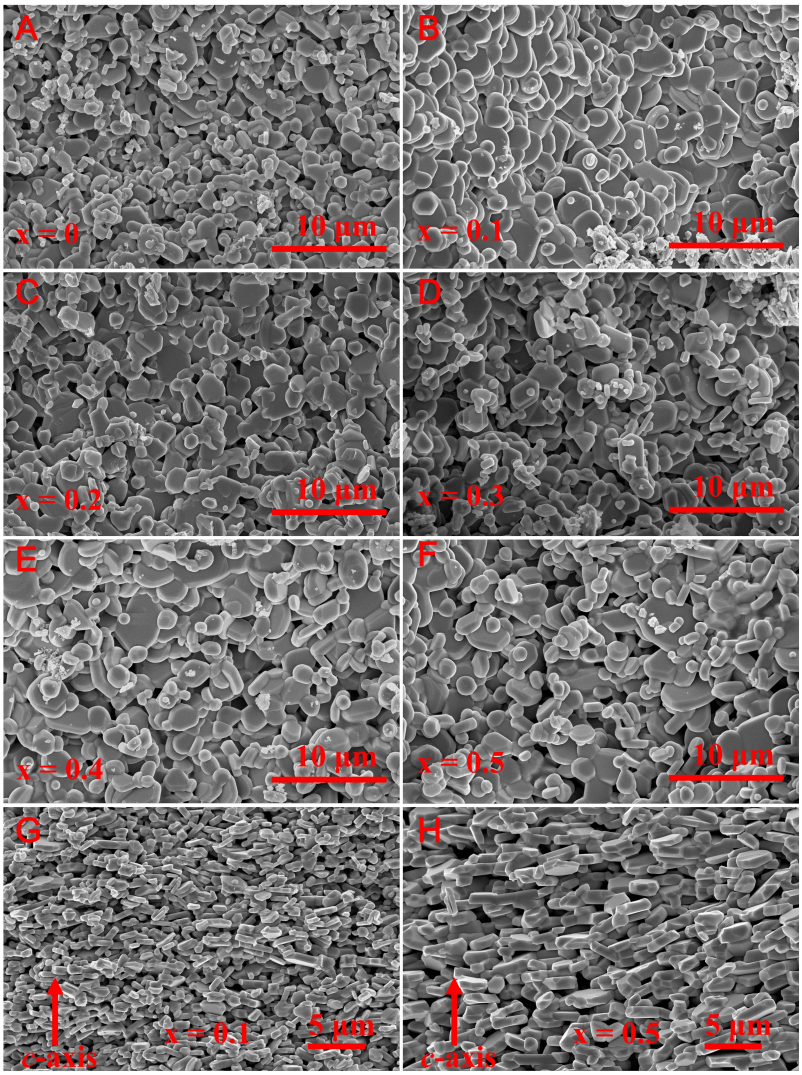

Figure 5. Microscopic morphology of oriented $Ba(ZnTi)_xFe_{12-2x}O_{19}$ hexaferrites. Panels (A-F) show the surface morphology for x = 0.0 - 0.5, while panels (G) and (H) show cross-sectional images for x = 0.1 and x = 0.5, respectively.

the grains tend to develop mainly along the direction normal to the sample surface. As shown in Figure 5G, the x = 0.1 sample displays noticeably more compact grain packing with fewer visible voids than the x = 0.5 sample shown in Figure 5H, which is in good agreement with its higher bulk density and lower porosity values listed in Table 1. As shown in Figure 6, the grain size distributions for both compositions exhibit a pronounced concentration, confirming their uniform grain size. Statistical analysis in Figure 6A-F indicates an overall trend of an initial increase and subsequent decrease in the average grain size, despite some irregular fluctuations.

Raman spectroscopy analysis

Raman spectroscopy arises from the inelastic scattering of incident photons by material constituents, a process that involves energy transfer. This method is capable of probing local structural features, such as vibrational modes and bond strengths[20]. Group theory analysis based on D_{6h} symmetry indicates that M-type hexaferrites possess 42 Raman-active modes ($11A_{1g} + 14E_{1g} + 17E_{2g}$), 30 infrared-active modes ($13A_{2u} + 17E_{1u}$), and 54 silent modes ($3A_{1u} + 4A_{2g} + 13B_{1g} + 4B_{1u} + 3B_{2g} + 12B_{2u} + 15E_{2u}$). The letters A, B, and E label different optical modes, while the subscripts g (gerade) and u (ungerade) indicate whether a given mode is symmetric or antisymmetric with respect to the inversion center[21,22].

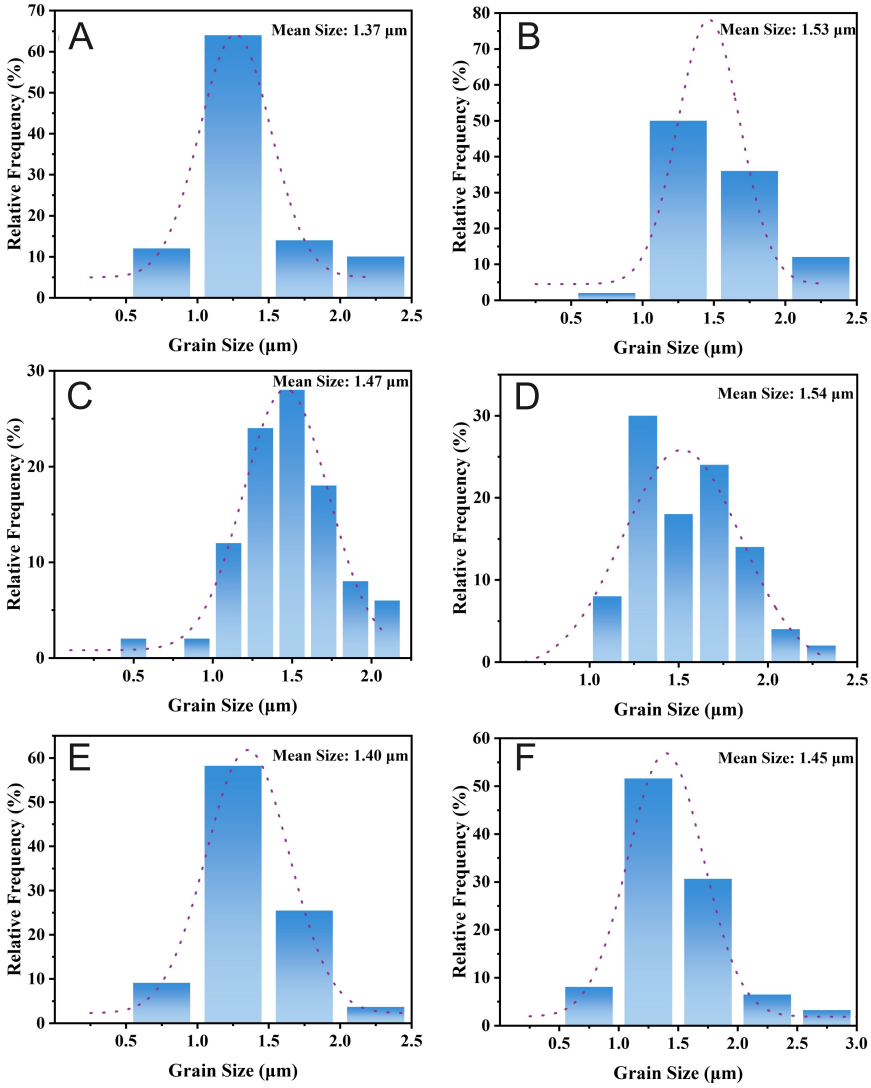

Figure 6. Grain size of oriented $Ba(ZnTi)_xFe_{12-2x}O_{19}$: (A-F) hexaferrites surface at x = 0.0 - 0.5.

As shown in Figure 7A, the BaM crystal structure consists of alternating rhombohedral (R) and spinel (S) blocks stacked along the *c*-axis. This arrangement is conventionally denoted as RSR^*S^*, where the asterisk indicates a 180° rotation of the corresponding block about the *c*-axis[13]. Within the oxygen interstices of the R and S blocks, Fe^{3+} ions occupy five distinct crystallographic sites: three octahedral sites (2a, 12k, $4f_2$), one bipyramidal site (2b), and one tetrahedral site ($4f_1$), among which 2a, 12k, and 2b spin up, while $4f_1$ and $4f_2$ spin down[23].

For M-type hexaferrites, the octahedra (FeO_6), bipyramids (FeO_5), and tetrahedra (FeO_4) each give rise to characteristic Raman vibration modes. The Raman spectra acquired from our samples in the range of 100-800 cm^{-1} are presented in Figure 7B. Their peak positions and intensities agree well with the literature values for typical BaM[18]. Furthermore, Figure 7C depicts the result of applying a Gaussian fit to the Raman spectrum. The major Raman peak parameters, such as frequencies (Freq) and intensities (cts), are summarized in Table 2 based on the fitting results. The Raman peaks corresponding to the tetrahedral ($4f_1$) and octahedral ($4f_2$) sites show the most pronounced trend: as x increases, the peak intensity (cts) generally decreases, indicating that Zn^{2+}-Ti^{4+} preferentially substitute Fe^{3+} at these lattice positions. This substitution disrupts crystal symmetry, increases disorder, and induces local strain[24]. No additional peaks are observed in

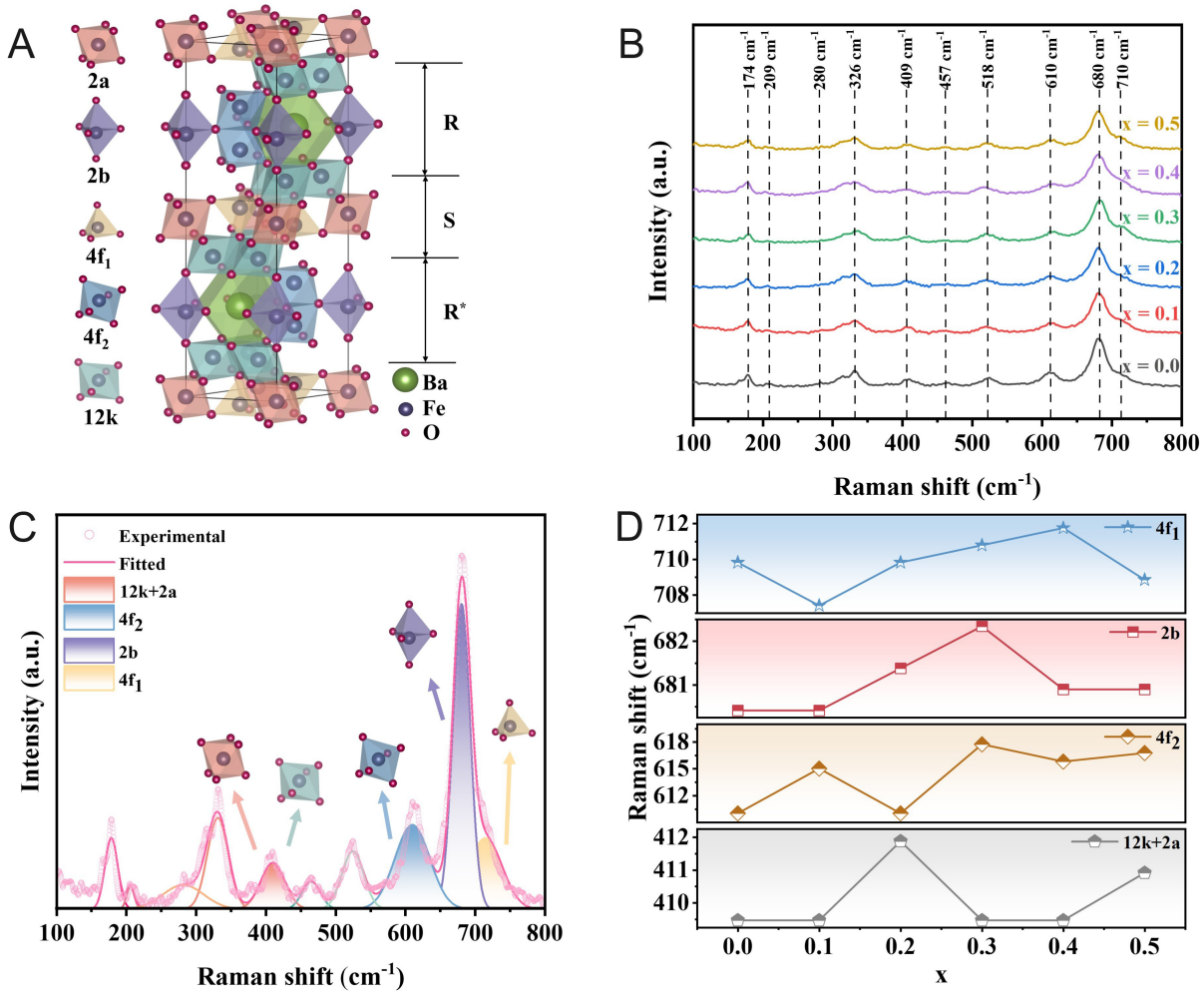

Figure 7. (A) Crystal structures of BaM ($BaFe_{12}O_{19}$); (B) Raman spectra of $Ba(ZnTi)_xFe_{12-2x}O_{19}$; (C) Fitted Raman spectrum of $Ba(ZnTi)_xFe_{12-2x}O_{19}$ (x = 0.0); (D) The Raman shifts of five sites as a function of Zn^{2+}-Ti^{4+} substitution.

the Raman spectra, confirming the phase purity of the samples and consistent with the XRD results.

Figure 7D presents a more detailed view of the Raman shifts of the five crystallographic sites as a function of Zn^{2+}-Ti^{4+} substitution. As x increases, the Raman vibrational modes associated with the $4f_1$ and $4f_2$ sites show a noticeable shift. However, the mode positions corresponding to the remaining sites, namely 12k, 2a, and 2b, remain essentially unchanged until x reaches 0.1. It suggests that Zn^{2+}-Ti^{4+} initially occupy the $4f_1$ and $4f_2$ sites in BaM. Although Raman spectroscopy probes local bonding environments and does not directly measure cation site occupancy, the clear shifts observed in the vibrational modes of the $4f_1$ and $4f_2$ polyhedra strongly suggest that these two sites are the most affected by the introduction of Zn^{2+} and Ti^{4+} ions into the BaM lattice. As discussed in the Introduction, the site preference of Ti^{4+} in M-type hexaferrites remains unsettled. The site-occupation tendencies for Zn^{2+} and Ti^{4+} inferred from these Raman shifts are qualitatively consistent with the model proposed by González-Angeles *et al.*[10]. According to this model, Zn^{2+} and Ti^{4+} tend to occupy the $4f_1$ and $4f_2$ sites, respectively, thereby reducing the spin-down contribution and leading to an initial enhancement of the saturation magnetization. Upon further increase in x, Raman shifts are observed for all five sites, indicating that Zn^{2+}-Ti^{4+} progressively occupy all five positions.

Based on the site occupation evolution revealed by Raman spectroscopy, the non-monotonic variations of both the (203) diffraction peak angle in Figure 3C and the lattice parameters in Table 1 can be understood in terms of site occupation preference and doping level. For x = 0.1, where Zn^{2+} and Ti^{4+} preferentially occupy

Table 2. Observed frequency (Freq) and Counts (cts) of Raman peaks of $Ba(ZnTi)_xFe_{12-2x}O_{19}$ (x = 0.0 - 0.5)

Associated polyhedra	Symmetry	Item	x = 0.0	x = 0.1	x = 0.2	x = 0.3	x = 0.4	x = 0.5
Whole spinel blocks	E_{1g}	Freq	174	176	177	178	175	176
		cts	28.04	25.76	24.36	20.77	21.81	20.22
O-Fe-O bridge	A_{1g}	Freq	209	205	206	206	210	209
		cts	9.83	8.34	7.03	5.00	5.56	4.47
Octahedron (2a)	E_{1g}	Freq	280	287	284	282	283	284
		cts	9.20	10.29	10.80	9.12	7.02	6.78
Octahedron (mixed)	E_{2g}	Freq	326	328	330	330	327	326
		cts	40.75	38.79	36.81	32.75	33.06	27.19
Octahedron (12k + 2a)	A_{1g}	Freq	409	409	412	409	409	411
		cts	19.53	19.72	19.16	15.48	10.87	9.70
Octahedron (mixed)	A_{1g}	Freq	457	459	464	464	459	461
		cts	10.49	10.65	12.08	6.56	3.75	2.15
Octahedron (mixed)	E_{2g}	Freq	518	520	520	518	519	521
		cts	21.13	20.67	20.87	21.14	17.68	14.03
Octahedron ($4f_2$)	A_{1g}	Freq	610	615	610	618	616	617
		cts	37.05	34.27	30.51	25.67	26.90	18.92
Bipyramid (2b)	A_{1g}	Freq	680	680	681	682	680	680
		cts	124.29	120.57	121.46	114.43	105.39	103.97
Tetrahedron ($4f_1$)	A_{1g}	Freq	710	707	710	711	712	709
		cts	36.68	30.70	24.72	34.45	35.10	28.86

the $4f_1$ and $4f_2$ sites, the smaller Ti^{4+} substituting Fe^{3+} produces a dominant local contraction, leading to a slight right-shift of the (203) peak and relatively stable lattice parameters. For x = 0.2 and 0.3, the (203) peak continues to shift rightwards, and the lattice parameters show a slight further contraction, indicating that the contraction effect from Ti^{4+} remains dominant during this stage. For x = 0.4 and 0.5, the dopant ions gradually occupy all five Fe^{3+} sites. The larger Zn^{2+} (0.74 Å) now exerts a net expansion effect that overcomes the contraction from Ti^{4+}, causing the (203) peak to shift leftwards and the lattice parameters to expand, reaching their maximum at x = 0.5. The non-monotonic trends observed in both the lattice parameters and the (203) peak angle, therefore, directly reflect a transition from preferential site occupation at low doping levels to broad multi-site substitution at higher doping levels, driven by the competing size effects of the larger Zn^{2+} and the smaller Ti^{4+} ions[25].

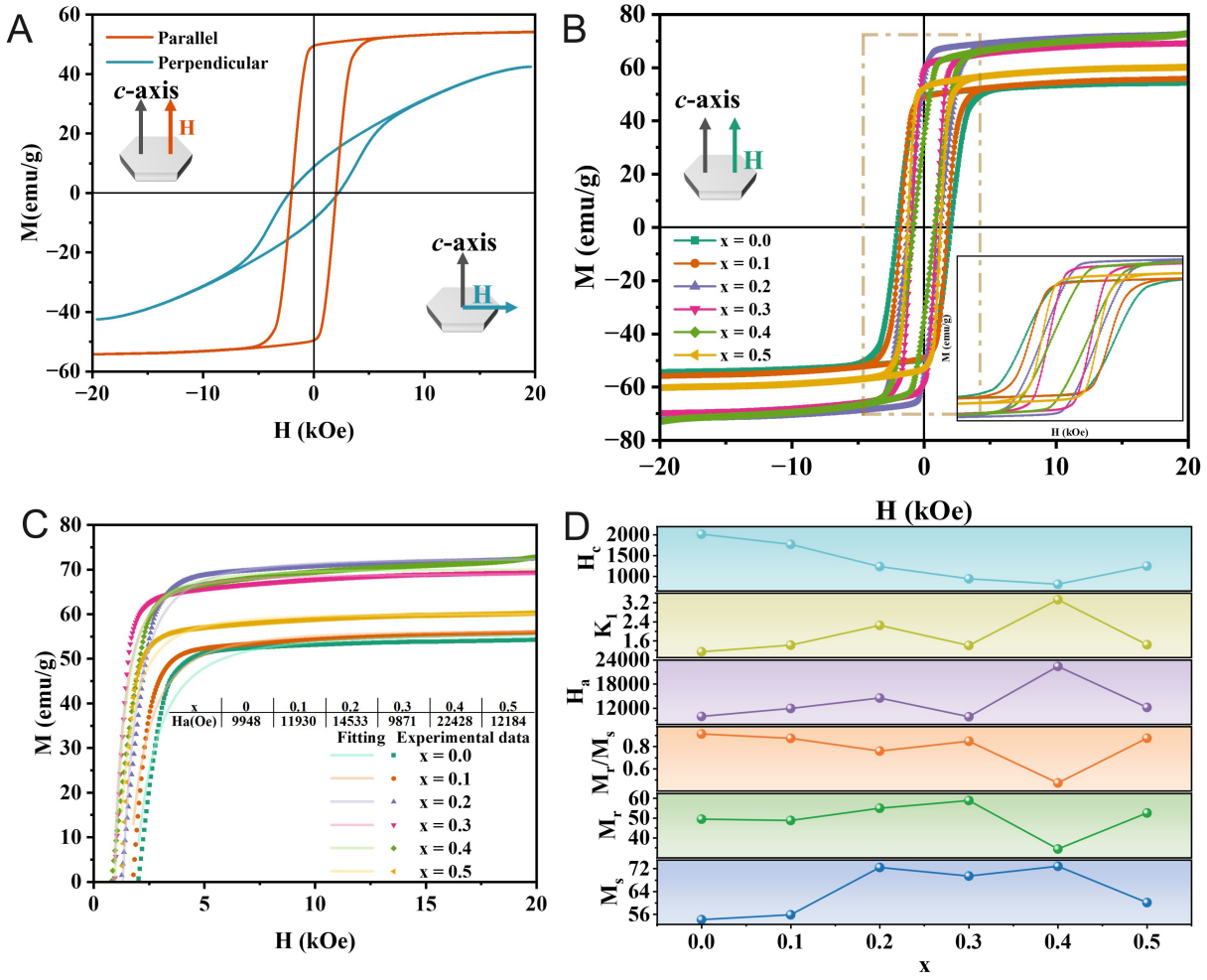

Figure 8. (A) Typical hysteresis loops of oriented $Ba(ZnTi)_xFe_{12-2x}O_{19}$ at x = 0.0; (B) Hysteresis loops of oriented $Ba(ZnTi)_xFe_{12-2x}O_{19}$ as functions of x; (C) The fitting lines of magnetic hysteresis loops along the easy axis according to the approaching saturation law; (D) Variation in magnetic properties as functions of x.

Static magnetic properties

Room-temperature magnetic characterization of the oriented samples was performed using a VSM. Figure 8A shows the hysteresis loops recorded for x = 0.0 under two field orientations: perpendicular and parallel to the hexagonal plane. When the magnetic field was applied perpendicular to the natural surface plane, which corresponds to the crystallographic easy axis, the sample reached magnetic saturation more readily. It showed a remanence ratio (M_r/M_s) of 0.91. This value is substantially higher than the theoretical upper limit of 0.5 expected for randomly oriented, non-interacting grains[13]. In contrast, when the field was applied parallel to the hexagonal plane along the hard axis, the remanence ratio fell sharply to just 0.20, and a much stronger applied field was needed before the sample reached saturation. These observations indicate that after magnetic-field alignment, the material displays strong direction-dependent magnetic anisotropy. Specifically, the anisotropy field is lower along the *c*-axis but higher within the basal plane. The hysteresis loops measured with the VSM field parallel to the *c*-axis for oriented samples at various x values are shown in Figure 8B. From these curves, we extracted the coercivity (H_c) and remanent magnetization (M_r) for each composition, and the results are compiled in Table 3.

When the applied field is sufficiently strong, the magnetization curves of polycrystalline magnetic materials gradually converge toward a common shape as the material approaches saturation. This behavior can be well described by the Law of Approach to Saturation (LAST) as follows[26].

Table 3. Magnetic parameters of oriented $Ba(ZnTi)_xFe_{12-2x}O_{19}$ (x = 0.0 - 0.5) hexaferrites

Sample	M_s (emu/g)	M_r (emu/g)	M_r/M_s	H_a (Oe)	K_1 (× 10^6 erg/cm³)	H_c (Oe)
x = 0.0	54.17	49.47	0.91	9948	1.15	2014
x = 0.1	55.84	48.80	0.87	11930	1.42	1769
x = 0.2	72.43	55.00	0.76	14533	2.25	1233
x = 0.3	69.43	58.85	0.84	9871	1.41	938
x = 0.4	72.84	34.37	0.47	22428	3.32	807
x = 0.5	60.12	52.61	0.87	12184	1.44	1245

$$M = M_S\left(1 - \frac{A}{H} - \frac{B}{H^2}\right) + \chi_p H \tag{4}$$

In Equation (4), the parameters A and B denote material-dependent coefficients with dimensions of Oe and Oe^2, respectively. They are associated with the resistance to magnetization during the technical magnetization process. Where χ_p denotes the paramagnetic susceptibility, and H is the applied magnetic field. For M-type hexaferrites, A is close to zero, and B is given as follows[27].

$$B = \frac{4K_1^2}{15\mu_0^2 M_S^2} = \frac{H_a^2}{15} \tag{5}$$

Here, μ_0 is the permeability of free space. In strongly magnetic materials like BaM, the paramagnetic susceptibility is sufficiently weak that the term $\chi_p H$ can be omitted[28]. Thus, the LAST expression can be simplified to the form given in Equation (6) as follows.

$$M = M_S\left(1 - \frac{B}{H^2}\right) \tag{6}$$

Here, M varies linearly with $1/H^2$. Under high-field conditions (19-20 kOe), the values of M_s, a material constant for a given composition, and B are obtained by linearly fitting M against $1/H^2$, as illustrated in Figure 8C. The anisotropy constant K_1 and the anisotropy field H_a are then determined using Equation (5)[29,30]. The corresponding magnetic parameters derived from the grain structure are summarized in Table 3, and the compositional variation trends of these parameters are shown in Figure 8D.

As seen in the data, the trends of H_a and K_1 are essentially identical, consistent with the theoretical expectation that a larger H_a corresponds to a larger K_1. The saturation magnetization (M_s) of the samples initially rises to a peak of 72.84 emu/g at x = 0.4, then declines. It should be noted that although the highest M_s (72.84 emu/g) is attained at x = 0.4, its remanence ratio drops sharply to 0.47 as shown in Table 3, which is unfavorable for self-biased operation. Therefore, M_s must be evaluated together with M_r/M_s when assessing composition suitability for self-biased circulators. All Zn-Ti substituted compositions show higher M_s values than their undoped counterparts. It suggests that the ionic composition plays a key role in determining the hysteresis loop shape and associated magnetic parameters[31]. This overall enhancement in M_s is primarily due to the preferential occupation of the tetrahedral $4f_1$ and octahedral $4f_2$ sites by non-magnetic Zn^{2+} and Ti^{4+} ions, which replace the original spin-down Fe^{3+} moments at these positions, reducing the total spin-down contribution and increasing the net magnetization. However, with increasing Zn^{2+}-Ti^{4+} substitution, both M_r and M_s show non-monotonic, irregular trends, with M_s peaking at x = 0.4, and then decreasing. These trends can be attributed to the site preference of the dopant ions and their different ionic radii relative to those of the host ions, which alter interatomic distances and consequently modify the superexchange interactions of Fe-O-Fe[32]. Such modifications lead to either an enhancement or a reduction in magnetic properties, thereby explaining the irregular changes in both M_r and M_s[30]. The remanence ratio (M_r/M_s)

reaches its maximum value of 0.87 after doping at x = 0.1 and x = 0.5. It is also reflected in the SEM images shown in Figure 5G and H, which reveal the most distinct and uniform layered morphology for $Ba(ZnTi)_xFe_{12-2x}O_{19}$ at these compositions, features generally associated with improved magnetic performance. Differences in cross-sectional morphology correlate with different M_r/M_s values. Specifically, a more pronounced layered structure is associated with a higher remanence ratio. The increase in M_r/M_s from the theoretical maximum of 0.5 for randomly oriented non-interacting grains to 0.87 is mainly due to the effective *c*-axis grain alignment achieved by magnetic-field orientation during pressing. The high Lotgering factors and the cross-sectional SEM images in Figure 5G and H confirm that the platelet-like grains are aligned perpendicular to the sample plane.

Coercivity (H_c) is a key parameter distinguishing hard from soft magnetic behavior. Its variation in polycrystalline ferrites can be understood using Equation (7)[27]:

$$H_c \propto \frac{K_1}{M_s D} \tag{7}$$

An increase in grain size D reduces the total grain boundary area and weakens the overall pinning effect, thus lowering H_c. However, a larger K_1/M_s ratio strengthens pinning and acts in the opposite direction[33]. In the samples studied here, the observed non-monotonic behavior of H_c, which first decreases and then increases, is governed by the competition between these two factors. The minimum H_c does not strictly coincide with the maximum grain size D because the K_1/M_s ratio varies considerably with composition. When this ratio decreases sufficiently, it becomes the dominant factor controlling pinning behavior, driving H_c to lower values even as the grain size decreases. The subsequent rise in H_c at higher substitution levels is then driven by the combined effect of increasing K_1/M_s and decreasing D.

Gyromagnetic properties

In polycrystalline hexaferrites, the total FMR linewidth ΔH can be expressed as the sum of intrinsic linewidth ΔH_i, magnetocrystalline anisotropy contribution ΔH_a, porosity-related contribution ΔH_p, and surface roughness contribution ΔH_{oth}[34,35], as follows.

$$\Delta H = \Delta H_i + \Delta H_a + \Delta H_p + \Delta H_{oth} \tag{8}$$

ΔH_i is typically negligible for M-type hexaferrites, while ΔH_{oth} can be minimized by careful surface polishing[36]. Therefore, the following analysis focuses mainly on ΔH_a and ΔH_p. Importantly, ΔH_a and ΔH_p are positively related to the crystalline anisotropy and porosity-induced linewidth broadening contributions[37]. Because the samples consist of polycrystalline assemblies of oriented grains, the experimentally measured ΔH reflects an average of the collective gyromagnetic response arising from a large number of individual crystallites. Figure 9A-D displays the FMR absorption spectra of the BaM sample (x = 0.1) obtained by sweeping the external field (H_0) at different frequencies (f). H_0 was applied perpendicular to the sample plane, parallel to the *c*-axis. The experimental data measured in the 64-67 GHz frequency range are plotted as circular markers. The orange curve represents a fit using a Gaussian (GaussAmp) lineshape, while the green curve corresponds to a Lorentzian fit. Quantitatively, the Gaussian fit yields a higher coefficient of determination (R^2 = 0.975) than the Lorentzian fit (R^2 = 0.968) for the 64 GHz spectrum, indicating a better agreement with the experimental data. Therefore, the FMR linewidth (ΔH) was extracted from the Gaussian fit. The FMR peak position shifts with the external field across different frequencies.

To comprehensively evaluate the effect of Zn^{2+}-Ti^{4+} co-substitution on high-frequency magnetic losses, the FMR linewidths of all compositions (x = 0.0 - 0.5) were measured across the 40-67 GHz range. Figure 10 summarizes the dependence of ΔH on substitution level x, where ΔH was measured at a representative

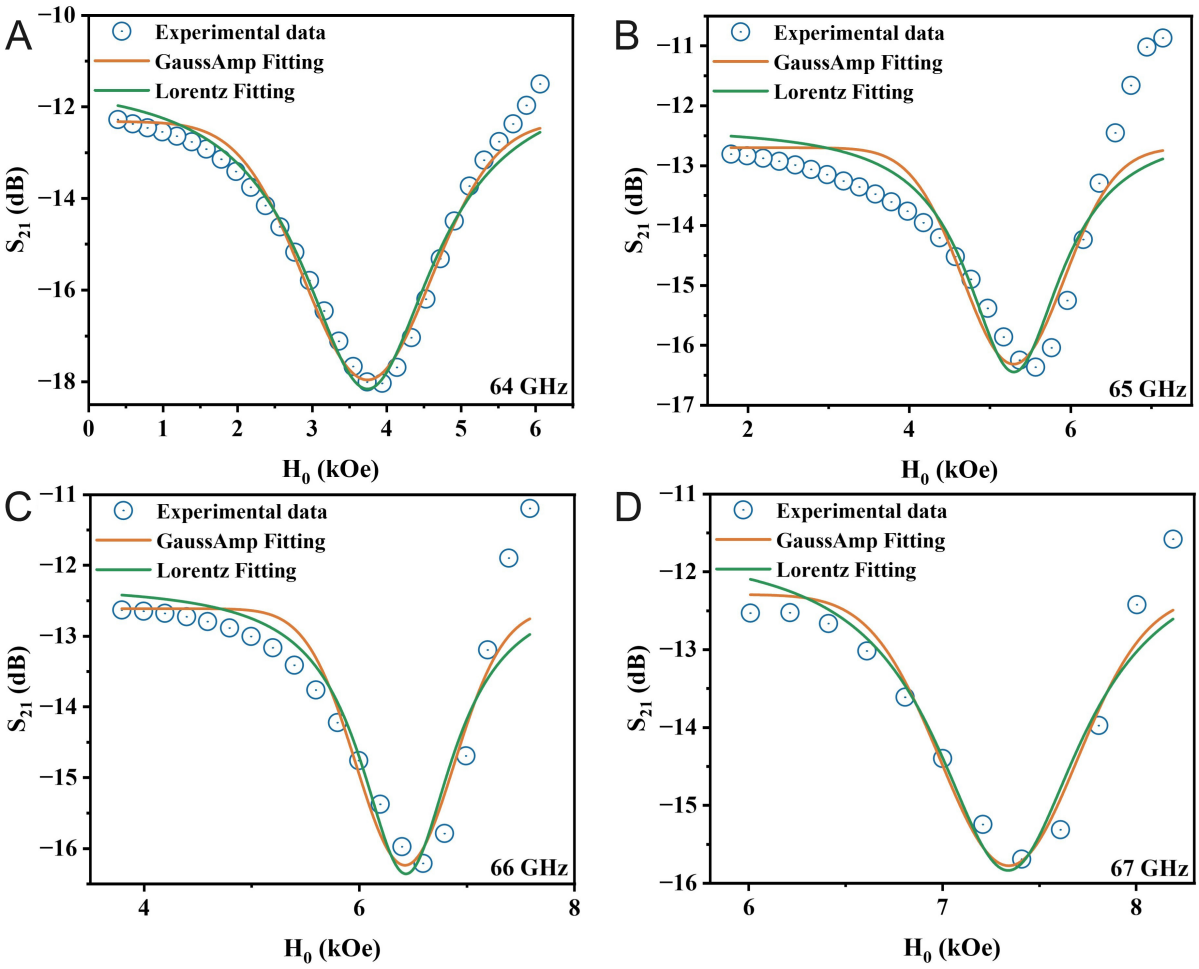

Figure 9. FMR absorption spectra of the BaM sample (x = 0.1) measured by sweeping the external field at different frequencies: (A) 64 GHz, (B) 65 GHz, (C) 66 GHz, and (D) 67 GHz. FMR: Ferromagnetic resonance.

frequency for each sample. The ΔH exhibits a clear non-monotonic trend where it initially decreases with increasing x, reaches a minimum at x = 0.2, and then increases significantly at higher substitution levels. Specifically, the narrowest linewidth of 289 Oe was achieved at 59 GHz for x = 0.2, while the broadest linewidth of 1,322 Oe was observed at 48 GHz for x = 0.5.

To quantitatively evaluate the role of porosity, Table 1 lists the porosity p of each oriented BaM sample. A direct comparison of the porosity data with the ΔH values shown in Figure 10 reveals a clear correlation between the two, as both quantities follow the same trend with increasing x and reach their lowest values at x = 0.2. As x increases beyond 0.3, porosity rises sharply to 18.70% at x = 0.5, accompanied by a sharp increase of ΔH to 1,322 Oe (at 48 GHz). In addition to porosity, the magnetocrystalline anisotropy field H_a also plays a role. As listed in Table 3, the H_a values for x = 0.1 (11,930 Oe) and x = 0.2 (14,533 Oe) are among the lower levels across all substituted samples, especially when compared with the much higher value at x = 0.4 (22,428 Oe). A lower anisotropy field generally reduces the anisotropy-related linewidth broadening contribution. Combining the two factors above, the narrow FMR linewidths observed at x = 0.1 (355 Oe at 67 GHz) and x = 0.2 (289 Oe at 59 GHz) can be attributed to the synergistic effect of minimal porosity and relatively low magnetocrystalline anisotropy field.

For a finite rectangular plate sample, the internal demagnetizing field $H_d = -N_z \cdot M_s$ is spatially nonuniform, where N_z is the position-dependent demagnetizing factor and M_s the saturation magnetization, due to

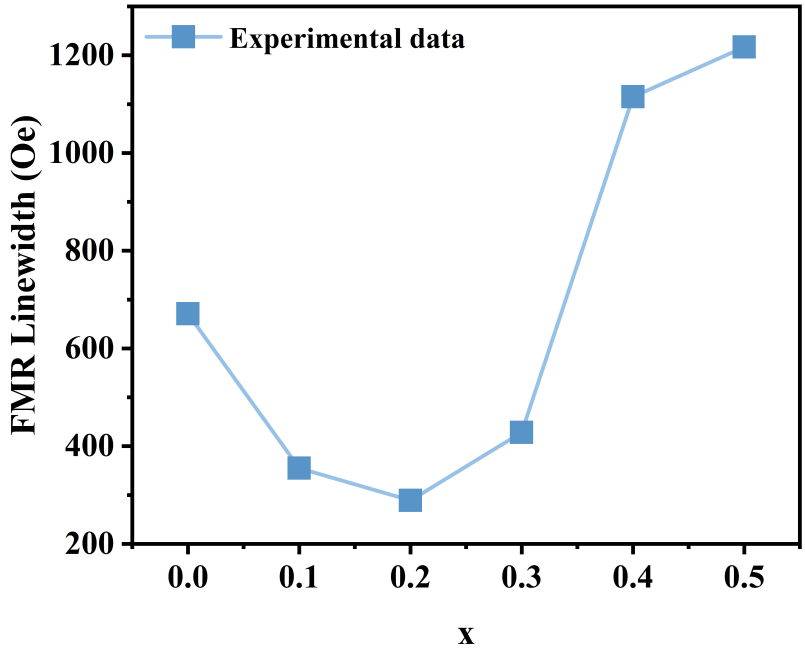

Figure 10. The dependence of ΔH on the substitution level x.

magnetic surface charges at the sample boundaries[38]. For the 4.0 × 4.0 × 0.8 mm³ specimens measured here ($M_s \approx 344$ emu/cm³, x = 0.2), a surface-integral calculation yields $N_z = 0.825$ at the center, decreasing to approximately 0.47 at the edge midpoint and approximately 0.41 near the corners. The standard deviation of the internal field across the midplane is approximately 40 Oe, contributing approximately 14% to the narrowest FMR linewidth ($\Delta H_{min} = 289$ Oe). Within the central 70% of the sample area, the field variation is only about 12 Oe, which is approximately 4% of ΔH_{min}. The edge demagnetizing effect is therefore a measurable but non-dominant source of linewidth broadening in our samples.

Compared with typical values for commercially available polycrystalline hexaferrites (~2,000 Oe)[39], all substituted samples in this study, especially those with x = 0.1 - 0.3, demonstrate markedly lower linewidths in the millimeter-wave band. Notably, the $Ba(ZnTi)_xFe_{12-2x}O_{19}$ hexaferrite with x = 0.2 exhibits the narrowest FMR linewidth of 289 Oe at 59 GHz, compared with previously reported values as shown in Figure 11. Among the investigated compositions, the x = 0.2 sample achieves the narrowest FMR linewidth in this study ($\Delta H = 289$ Oe at 59 GHz), underscoring the effectiveness of Zn-Ti co-substitution in suppressing magnetic losses. For practical self-biased circulator applications, the x = 0.1 composition offers the most well-rounded set of properties, as it simultaneously delivers the highest remanence ratio among all substituted samples at $M_r/M_s = 0.87$, a sufficiently large anisotropy field $H_a = 11{,}930$ Oe for millimeter-wave self-biasing, and a narrow FMR linewidth $\Delta H = 355$ Oe at 67 GHz that compares favorably with most reported values for polycrystalline M-type hexaferrites.

CONCLUSION

This study aimed to develop M-type hexaferrites with large magnetocrystalline anisotropy and narrow ferromagnetic resonance linewidth for millimeter-wave self-biased circulator applications. Zn-Ti co-substitution is an effective strategy for tailoring both the static and dynamic magnetic properties of *c*-axis-oriented BaM ceramics, enabling the simultaneous achievement of a high anisotropy field, an excellent squareness ratio, and a markedly reduced FMR linewidth. The best-performing compositions show an FMR linewidth substantially lower than that of commercial polycrystalline hexaferrites, while still maintaining the

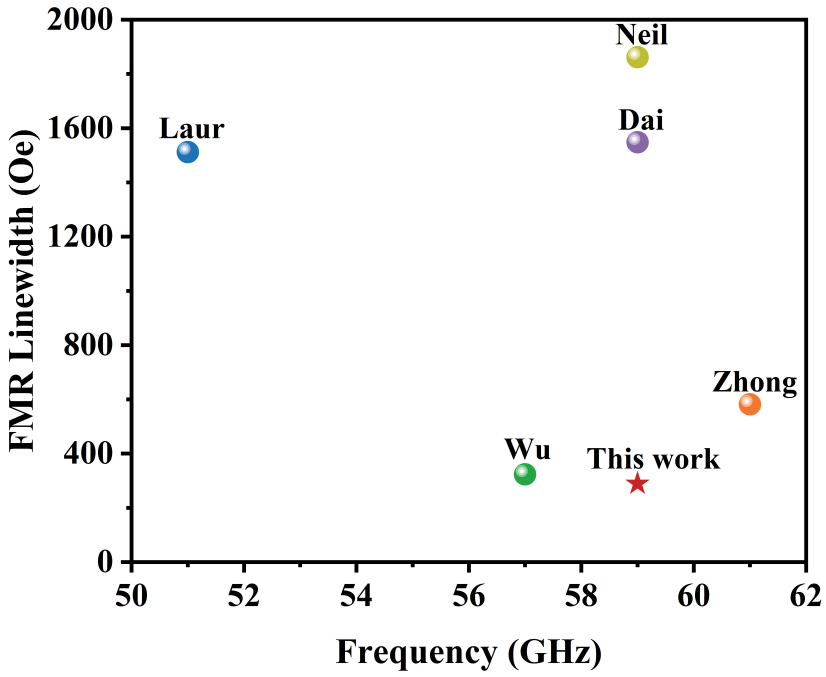

Figure 11. Published values of FMR linewidth in hexaferrites[40-44]. FMR: Ferromagnetic resonance.

strong uniaxial anisotropy required for effective self-biasing. These results indicate that Zn-Ti co-substituted, textured BaM hexaferrites are promising gyromagnetic materials for compact, low-loss circulators operating in the millimeter-wave band.

DECLARATIONS

Authors' contributions

Writing - original draft, methodology: Liao, Y.
Writing review & editing, resources: Liu, Q.
Software: Li, Z.; Tan, X.; Lai, Y.
Methodology: Wu, Y.; Chen, H.; Li, C.
Software, resources: You, X.; Wu, C.

Availability of data and materials

The raw data supporting the findings of this study, including XRD patterns, Raman spectra, SEM images, VSM hysteresis loops, and FMR absorption spectra, are available from the corresponding author (Liu, Q. liuq@cdut.edu.cn) upon reasonable request. All processed data are presented in the main text and accompanying figures and tables.

AI and AI-assisted tools statement

During the preparation of this manuscript, the AI tool DeepSeek-R1 (version initial release, released 2025-01-20) was used solely for language polishing and grammar refinement. The tool did not influence the study design, data collection, analysis, interpretation, or the scientific content of the work. All authors take full responsibility for the accuracy, integrity, and final content of the manuscript.

Financial support and sponsorship

This work is supported by the Sichuan Science and Technology Program [grant numbers: 2025ZNSFSC1384] and National Natural Science foundation of China [Nos: 52502330].

Conflicts of interest

All authors declared that there are no conflicts of interest.

Ethical approval and consent to participate

Not applicable.

Consent for publication

Not applicable.

Copyright

REFERENCES

1. Rathod, S.; Sreenivasulu, K.; Beenamole, K.; Ray, K. Evolutionary trends in transmit/receive module for active phased array radars. *Def. Sci. J.* **2018**, *68*, 553. DOI
2. Kodak, U.; Rebeiz, G. M. A 5G 28-GHz common-leg T/R front-end in 45-nm CMOS SOI with 3.7-dB NF and -30-dBc EVM with 64-QAM/500-MBaud modulation. In *EEE Transactions on Microwave Theory and Techniques*, 2019; Vol. 67, pp. 318-31. DOI
3. Tee, Y. T.; Seng, Y. H.; Boon, L. P.; et al. Design techniques to combat process, temperature and supply variations in Bluetooth RFIC. In *IEEE MTT-S International Microwave Symposium Digest, 2003*; Philadelphia, PA, USA, 2003; Vol. 1, pp. A37-A40. DOI
4. Wu, C.; Wang, W.; Li, Q.; et al. Barium hexaferrites with narrow ferrimagnetic resonance linewidth tailored by site-controlled Cu doping. *J. Am. Ceram. Soc.* **2022**, *105*, 7492-501. DOI
5. Trukhanov, A.; Kostishyn, V.; Panina, L.; et al. Magnetic properties and Mössbauer study of gallium doped M-type barium hexaferrites. *Ceram. Int.* **2017**, *43*, 12822-7. DOI
6. de Julian Fernandez, C.; Sangregorio, C.; de la Figuera, J.; Belec, B.; Makovec, D.; Quesada, A. Topical review: progress and prospects of hard hexaferrites for permanent magnet applications. *J. Phys. D. Appl. Phys.* **2021**, *54*, 153001. DOI
7. Xiang, X.; Yang, Z.; Fang, G.; et al. Tailoring tactics for optimizing microwave absorbing behaviors in ferrite materials. *Mater. Today. Phys.* **2023**, *36*, 101184. DOI
8. Qin, C.; Liu, R.; Sun, Y.; Wu, J.; Zhao, T.; Gong, H. Corrigendum to "Phase formation and magnetic properties of M-type lanthanum substituted strontium ferrites" [Ceram. Int. 49 (2023) 30924-30936]. *Ceram. Int.* **2023**, *49*, 41022. DOI
9. Mathews, S. A.; Babu, D. R. Analysis of the role of M-type hexaferrite-based materials in electromagnetic interference shielding. *Curr. Appl. Phys.* **2021**, *29*, 39-53. DOI
10. González-angeles, A.; Mendoza-suarez, G.; Grusková, A.; Papánová, M.; Slama, J. Magnetic studies of Zn-Ti-substituted barium hexaferrites prepared by mechanical milling. *Mater. Lett.* **2005**, *59*, 26-31. DOI
11. Wartewig, P.; Krause, M.; Esquinazi, P.; Rösler, S.; Sonntag, R. Magnetic properties of Zn- and Ti-substituted barium hexaferrite. *J. Magn. Magn. Mater.* **1999**, *192*, 83-99. DOI
12. Solizoda, I.; Zhivulin, V.; Zirnik, G.; et al. Influence of Ti/Al substitution on the structural features, magneitc properties and THz characteristics of M-type hexaferrites. *Ceram. Int.* **2025**, *51*, 2811-20. DOI
13. Pullar, R. C. Hexagonal ferrites: a review of the synthesis, properties and applications of hexaferrite ceramics. *Prog. Mater. Sci.* **2012**, *57*, 1191-334. DOI
14. Baniasadi, A.; Ghasemi, A.; Nemati, A.; Azami Ghadikolaei, M.; Paimozd, E. Effect of Ti-Zn substitution on structural, magnetic and microwave absorption characteristics of strontium hexaferrite. *J. Alloys. Compd.* **2014**, *583*, 325-8. DOI
15. Almessiere, M.; Slimani, Y.; Tashkandi, N.; et al. The effect of Nb substitution on magnetic properties of $BaFe_{12}O_{19}$ nanohexaferrites. *Ceram. Int.* **2019**, *45*, 1691-7. DOI
16. Lu, S.; He, Y.; Liu, Y. Structural and magnetic studies of textured hexagonal ferrite $BaFe_{12-x}(ZnHf)_xO_{19}$. *J. Alloys. Compd.* **2026**, *1062*, 187275. DOI
17. Lu, S.; Liu, Y.; Yin, Q.; Chen, J.; Wu, J.; Li, J. Enhanced magnetic properties of $Sr_{0.7}Ce_{0.3}Fe_{11.7}Zn_{0.3}O_{19}$ by tuning pre-sintering temperature. *J. Alloys. Compd.* **2023**, *941*, 168833. DOI
18. Lu, S.; Liu, Y.; Yin, Q.; et al. Investigation of crystal structure, Raman spectroscopy and magnetic properties of La-Zn substituted oriented M-type hexagonal barium ferrites. *Mater. Res. Bull.* **2024**, *172*, 112640. DOI
19. Liu, K.; Wang, Q.; Wu, Q.; Zhang, F.; Li, L.; Zheng, H. Cu-Sn co-doped M-type barium ferrites: magnetism, dielectric properties, and ferromagnetic resonance linewidth. *Ceram. Int.* **2025**, *51*, 28726-35. DOI
20. Xu, Y.; Aljuhani, W.; Zhang, Y.; Ye, Z.; Li, C.; Bell, S. E. J. A practical approach to quantitative analytical surface-enhanced Raman spectroscopy. *Chem. Soc. Rev.* **2025**, *54*, 62-84. DOI
21. Buzinaro, M.; Ferreira, N.; Cunha, F.; Macêdo, M. Hopkinson effect, structural and magnetic properties of M-type Sm^{3+}-doped $SrFe_{12}O_{19}$ nanoparticles produced by a proteic sol-gel process. *Ceram. Int.* **2016**, *42*, 5865-72. DOI

22. Kreisel, J.; Lucazeau, G.; Vincent, H. Raman spectra and vibrational analysis of $BaFe_{12}O_{19}$ hexagonal ferrite. *J. Solid. State. Chem.* **1998**, *137*, 127-37. DOI
23. Chen, Z.; Liu, Y.; Lu, S.; et al. Ga-induced tuning of structural and magnetic properties in BaM hexaferrites for self-biased microwave circulators. *Ceram. Int.* **2025**, *51*, 58951-9. DOI
24. Chen, Z.; Liu, Y.; Lu, S.; et al. Effect of Zn^{2+}-Zr^{4+} co-substitution on grain growth and magnetic properties of c-axis oriented M-type hexaferrites. *Ceram. Int.* **2025**, *51*, 7358-69. DOI
25. Lee, K.; Kang, Y.; Yoo, S. Effects of La-Co Co-substitution on the structural and magnetic properties of SrM hexaferrites prepared by solid-state reaction. *Appl. Sci.* **2024**, *14*, 848. DOI
26. Zhang, H.; Zeng, D.; Liu, Z. The law of approach to saturation in ferromagnets originating from the magnetocrystalline anisotropy. *J. Magn. Magn. Mater.* **2010**, *322*, 2375-80. DOI
27. Chen, Z.; Liu, Y.; Lu, S.; et al. Mechanisms of chromium (Cr) doping on crystal structure and magnetic properties of oriented polycrystalline M-type hexaferrites: a comprehensive study using multiple materials characterization techniques. *J. Alloys. Compd.* **2025**, *1036*, 181854. DOI
28. Qin, C.; Sun, Y.; Li, Z.; et al. Effect of Fe deficiency on the crystalline structure and magnetic properties of M-type strontium hexaferrite. *Arab. J. Chem.* **2023**, *16*, 105092. DOI
29. Akhtar, M. N.; Rahman, A.; Sulong, A.; Khan, M. A. Structural, spectral, dielectric and magnetic properties of $Ni_{0.5}Mg_xZn_{0.5-x}Fe_2O_4$ nanosized ferrites for microwave absorption and high frequency applications. *Ceram. Int.* **2017**, *43*, 4357-65. DOI
30. Li, C.; Liu, Q.; Tan, X.; et al. Boosting gyromagnetic performance of W-type hexaferrite through Bi_2O_3-induced liquid-phase sintering. *Ceram. Int.* **2025**, *51*, 56508-16. DOI
31. Azhar Khan, M.; Aslam, S.; Asif Iqbal, M.; et al. Structural spectral, dielectric, and magnetic properties of Mg substituted Ba3CoFe24O41 Z-type hexaferrites. *J. Magn. Magn. Mater.* **2022**, *560*, 169589. DOI
32. Trukhanov, S.; Trukhanov, A.; Turchenko, V.; et al. Polarization origin and iron positions in indium doped barium hexaferrites. *Ceram. Int.* **2018**, *44*, 290-300. DOI
33. Tan, X.; Liu, Q.; Li, C.; et al. Phase formation, microstructure and magnetic properties of X-type hexaferrite based composite for microwave applications. *Ceram. Int.* **2025**, *51*, 17172-80. DOI
34. Li, Q.; Wang, J.; Yao, H. Soft magnetic, gyromagnetic, and microstructural properties of BBSZ-Nb_2O_5 doped NiCuZn ferrites for LTCC applications. *Ceram. Int.* **2022**, *48*, 8653-60. DOI
35. Lei, Y.; Liu, K.; Huo, X.; et al. Effect of Sr^{2+} and Cr^{3+} co-doping on the microstructure and high-frequency electromagnetic properties of M-type barium hexaferrites for microwave applications. *Ceram. Int.* **2025**, *51*, 22317-26. DOI
36. Yang, W.; Qian, Y.; Zheng, H. Hot press sintering of Bi-Zn-In-Sn doped yttrium iron garnet ferrite: magnetism, ferromagnetic resonance linewidth and dielectric properties. *Ceram. Int.* **2025**, *51*, 23779-87. DOI
37. Lei, Y.; Liu, K.; Huo, X.; et al. Tailored magnetic and microwave characterizations of La-Al doped BaM hexaferrites for millimeter-wave band applications. *J. Alloys. Compd.* **2025**, *1042*, 183968. DOI
38. Mu, Y.; Yi, Y.; Zhu, W.; Zhang, M. Numerical calculation method of shape demagnetization tensor spatially profile for cuboid. *Phys. Scr.* **2025**, *100*, 045008. DOI
39. Akaiwa, Y.; Okazaki, T. An application of a hexagonal ferrite to a millimeter-wave Y circulator. In *IEEE Transactions on Magnetics*, 1974; Vol. 10, pp. 374-8. DOI
40. O'neil, B.; Young, J. Experimental investigation of a self-biased microstrip circulator. In *IEEE Transactions on Microwave Theory and Techniques*, 2009; Vol. 57, pp. 1669-74. DOI
41. Dai, Y.; Lan, Z.; Yu, Z.; et al. Effects of La substitution on micromorphology, static magnetic properties and low ferromagnetic resonance linewidth of self-biased M-type Sr hexaferrites for high frequency application. *Ceram. Int.* **2021**, *47*, 8980-6. DOI
42. Laur, V.; Verissimo, G.; Queffelec, P.; et al. Self-biased Y-junction circulators using lanthanum- and cobalt-substituted strontium hexaferrites. In *IEEE Transactions on Microwave Theory and Techniques*, 2015; Vol. 63, pp. 4376-81. DOI
43. Zhong, L.; Lan, Z.; Li, Q.; et al. Synergetic effect of site-controlled two-step Ca doping on magnetic and electrical properties of M-type strontium hexaferrites. *J. Eur. Ceram. Soc.* **2023**, *43*, 5521-9. DOI
44. Wu, C.; Li, J.; Lan, Z.; et al. Crystallographically textured $Ba_{0.8}La_{0.2}Fe_{11.8-x}Cu_{0.2}O_{19-\delta}$ hexaferrites with narrow FMR linewidth. *Ceram. Int.* **2020**, *46*, 8719-24. DOI